

Supplement of E&G Quaternary Sci. J., 68, 215–236, 2020  
<https://doi.org/10.5194/egqsj-68-215-2020-supplement>  
© Author(s) 2020. This work is distributed under  
the Creative Commons Attribution 4.0 License.



*Supplement of*

## **Sediment-filled karst depressions and *riyad* – key archaeological environments of south Qatar**

**Max Engel et al.**

*Correspondence to:* Max Engel ([max.engel@uni-koeln.de](mailto:max.engel@uni-koeln.de))

The copyright of individual parts of the supplement might differ from the CC BY 4.0 License.

## **S1 Methodological details of the magnetometer prospection**

For our purpose to reach the highest possible sensitivity, a maximum speed of prospection and to get additional information on the enrichment of magnetic minerals in lateral sediments layers we chose the Cs total field magnetometer (Scintrex SM4G-Special). We applied the instrument by the so-called “duo-sensor” configuration. By this configuration, probes are mounted on a wooden frame and carried in zigzag-mode c.  $30\pm 5$  cm above the ground (Fig. S11). The profiles of the 40 m x 40 m grids were oriented E–W in order to minimize technical disturbance and interactions of the magnetometer probes with the electronic parts and the batteries of the device. The sampling frequency of the magnetometer (10 readings per second) allows the survey of a 40 m profile in less than 30 s, maintaining the spatial resolution of data sampling (10 measurements per second) of approximately 10–15 cm by normal walking speed. Every 5 m, in parallel to the magnetic data, a manual switch sets a marker. This helps to perform the best and most exact interpolation of data during the subsequent processing work, where we remove the slight linear changes in the daily variation of the geomagnetic field by a reduction filter and calculate the mean value of the 40 m profile. Additionally, we calculate the mean value of all data of the grid and subtract this value from the survey data. Hereby, we assume that the variation of the Earth’s magnetic field during the measurement of one 40 m profile follows a linear increase or a linear decrease of the intensity of the Earth’s magnetic field. Thus, it is possible to eliminate this variation for each traverse line by a reduction to the mean line value. Alternatively, in magnetically quiet areas, it is also useful to calculate the mean value of the whole 40 m x 40 m grid and use this value for further data processing as described above. To create discrete field values we apply a resampling program setting the data to a sampling interval of 25 cm x 25 cm. Additionally, by using this procedure, the difference between the measurement of both the magnetometer probes and the theoretically calculated mean value of the Earth’s magnetic field is obtained. This intensity difference shows the apparent magnetic anomaly, caused by the magnetic properties of specific subsurface structures, the soil magnetism and the geology. The application of the optical pumped Cs magnetometer Smartmag in the duo-sensor configuration allows to set the reference value, e.g. the virtual gradient of the Earth’s magnetic field, to infinity in order to enable recording of the full intensity of the magnetic anomalies (Fassbinder, 2015, 2017).

The great advantage of this configuration (compared to fluxgate gradiometers) is rather obvious. The resulting data not only provide a higher magnetic intensity of the anomalies and, hence, more information on the buried features, but also on deeper parts of magnetically enriched layers, ash layers, palaeo-channels, archaeological structures and changes in depositional environments. The SM4G-Special magnetometer measures the total Earth’s magnetic field intensity by an intrinsic sensitivity of  $\pm 10.0$  pT with a sampling rate of ten measurements per second. For comparison: The daily fluctuations of the Earth’s magnetic field in Asaila (02/2014) varied within the range of c.  $43510\pm 20$  nT.

The data were stored as binary files on the read-out unit, then downloaded to a Panasonic Toughbook and unpacked to ASCII data. For image processing and further treatment of the data (resampling), we applied a special self-made software, the program Geoplot (Geoscan Ltd. UK) and Surfer (Golden Software, USA). The visualization as a grey scale image (magnetogram) permits to trace even negligible anomalies originating from the shade of slightly enriched sediment layers beneath the surface. The

application of a high-pass filter removes the deeper and mainly geological features and provides supplemental information on the type of the anomalies. The magnetometer measurements were complemented by magnetic susceptibility measurements on the topsoil and rocks on the site, conducted using a handheld magnetic susceptibility meter SM-30 by ZHstruments.

## **S2 Methodological details and results of the optically stimulated luminescence dating**

Samples were taken from closed sediment cores (QAT 63), which were opened in dark conditions under subdued red light at the Cologne Luminescence Laboratory (CLL), and a trench (QAT 41), where thick-walled, opaque PVC tubes were carefully hammered into the trench wall. Water content for the samples was either calculated as maximum pore water content for samples that were identified to be located below the groundwater table during the entire period after deposition (QAT 63-3), or measured after sampling for samples clearly above the present groundwater table (QAT 63-1); for QAT 63-2 both values were used to calculate minimum and maximum dose rates, since the sample has been and is currently affected by water-level variations. U, Th, and K contents of the samples were determined by means of high-resolution gamma spectrometry. Dose rates were calculated with the dose rate and age calculator (DRAC) software (Durcan et al., 2015) using the conversion factors of Guérin et al. (2011) and the contribution of cosmic radiation according to Prescott and Hutton (1994). Minimum and maximum dose rates for QAT 63-2 are based on measured and saturated water contents, respectively. Samples for burial dose determination were processed under subdued red light following standard procedures to extract coarse-grain quartz. Samples were sieved to fractions of 100–200  $\mu\text{m}$ , and treated with HCl (10%) and  $\text{H}_2\text{O}_2$  (10%) to remove carbonates and organic matter. Density liquid was used to separate quartz grains from feldspar and heavy minerals ( $2.62 < \text{quartz} < 2.68 \text{ g/cm}^3$ ). The alpha radiation-affected rim of the quartz grains and remaining feldspar contamination were removed by a final HF etch (40%) for 40 minutes. Large aliquots (8 mm diameter) of pure quartz grains were fixed on stainless steel discs using silicon spray. All dose measurements were performed on a Risø TL/DA 20 luminescence reader following a standard SAR (single aliquot regenerative dose) protocol (Murray and Wintle, 2003) with signal stimulation for 40 seconds using blue LEDs and signal detection through U340 filters. Preheat temperatures of 220–240 °C were experimentally determined by means of preheat-plateau tests (Fig. S1). Adequate performance of the protocol was evaluated on the basis of dose-recovery experiments (mean dose-recovery ratios of 0.95 to 1.01 for all samples; Fig. S2) and fitting of quartz signal components (all samples are dominated by the fast component; Fig. S3). A total of 20–47 aliquots per sample passed the acceptance criteria in terms of recycling ratio (0.9–1.1) and recuperation (<5% of the equivalent dose). Since the shape of the equivalent dose ( $D_e$ ) distributions (Fig. S4) and over-dispersion values of 9–24% point to more or less complete signal resetting for all samples, burial doses were calculated using the central age model (Galbraith et al., 1999). Dose rates, burial doses and ages of all samples are compiled in Table S1.

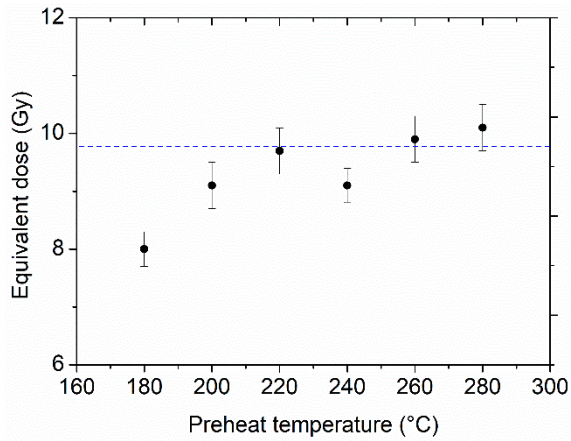


Fig. S1: Preheat-plateau test for sample QAT 63-2. Equivalent doses were determined with increasing preheat temperatures between 180 and 280 °C using four aliquots per temperature step. The mean equivalent doses form a plateau (blue dotted line) that indicates independence of thermal treatment for the temperature range 220–280 °C.

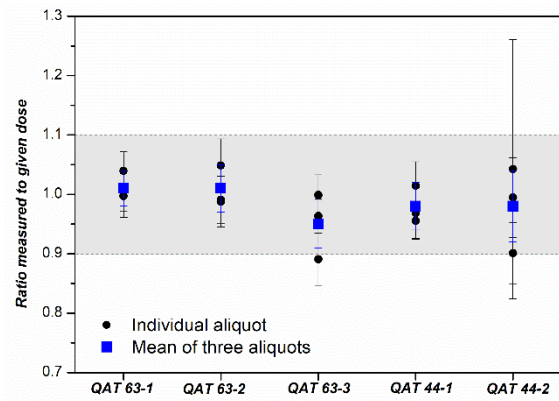


Fig. S2: Dose-recovery experiments for all samples. Three aliquots of each sample were bleached at room temperature with blue LEDs for 100 seconds, irradiated with a laboratory dose approximately equalling the burial dose, and measured using a standard SAR protocol. The mean dose-recovery ratios of all samples (blue squares) are in the acceptable range of 0.9–1.1.

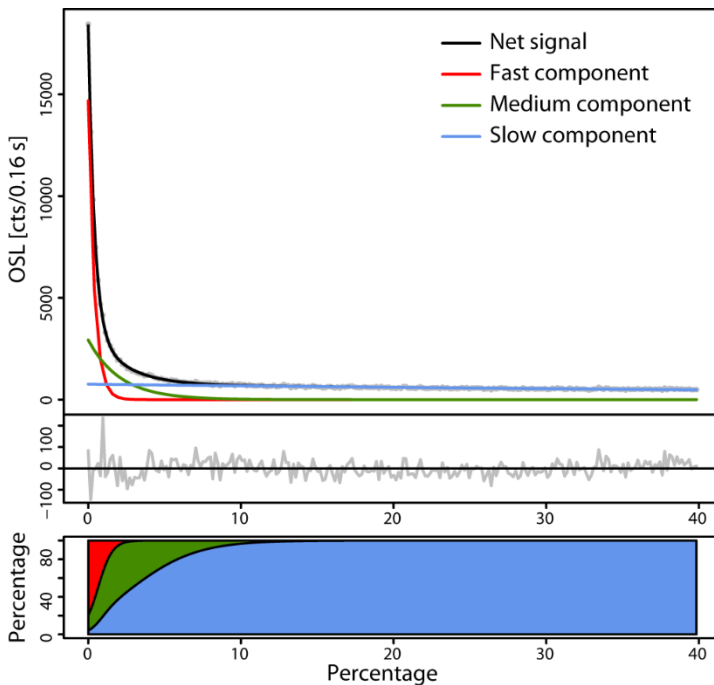


Fig. S3: Continuous wave OSL curve fitting for sample QAT 63-1. The first seconds of the quartz OSL signal, which are used for equivalent dose determination, are clearly dominated by the thermally stable and rapidly resetting fast component (red).

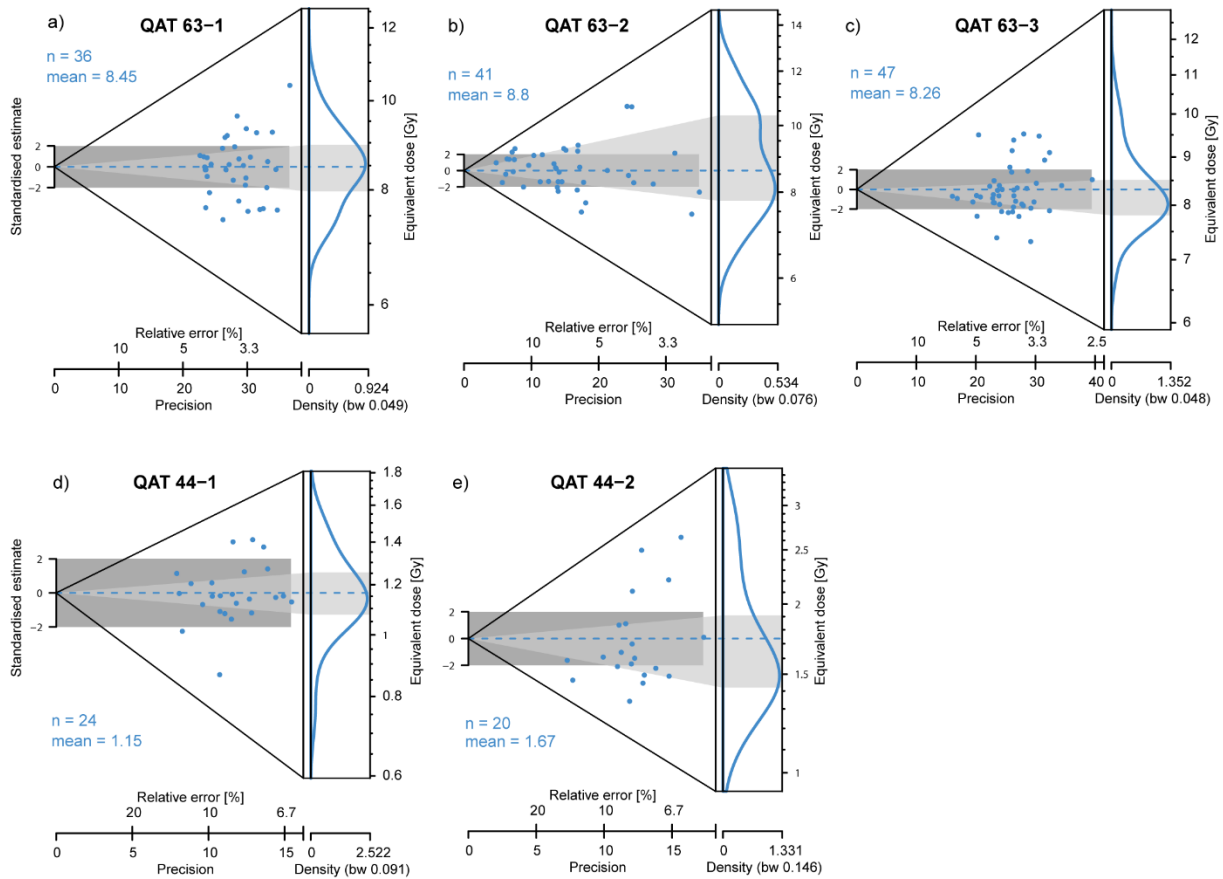


Fig. S4: Equivalent dose distributions of all samples shown as abanico plots.

Table S1: Compilation of OSL data for all five samples ( $DR_{tot}$ =environmental dose rate;  $n$ =number of accepted aliquots; OD=over-dispersion; De=equivalent dose). Measurements were carried out in the Cologne Luminescence Lab (CLL; lab code: C-L). Note that luminescence ages always refer to the year of sampling, in this case 2014. <sup>1</sup>For sample QAT 63-2, both measured and saturation water content were used for dose rate and age calculation.

Sample code	Lab code	Depth (m b.s.)	Grain size ( $\mu\text{m}$ )	U (ppm)	Th (ppm)	K (%)	Water (mass-%)	$DR_{tot}$ (Gy/ka)	n	OD (%)	De (Gy)	Age (years)
QAT 63-1	C-L3937	0.50	150-200	$0.84 \pm 0.05$	$1.26 \pm 0.11$	$1.07 \pm 0.02$	$7 \pm 5$	$1.45 \pm 0.06$	36	$8.8 \pm 0.4$	$8.46 \pm 0.14$	$5810 \pm 260$
QAT 63-2	C-L3938	1.75	150-200	$0.96 \pm 0.05$	$1.43 \pm 0.12$	$1.01 \pm 0.02$	$10 \pm 5^1$ ; $25 \pm 5$	$1.19 \pm 0.04^1$ ; $1.36 \pm 0.06$	43	$15 \pm 0.9$	$8.68 \pm 0.25$	$6397 \pm 320^1$ ; $7293 \pm 338$
QAT 63-3	C-L3939	2.75	150-200	$0.76 \pm 0.05$	$1.21 \pm 0.11$	$0.98 \pm 0.02$	$25 \pm 5$	$1.10 \pm 0.04$	47	$8.6 \pm 0.3$	$8.27 \pm 0.12$	$7506 \pm 294$
QAT 44-1	C-L4478	0.30	100-200	$1.23 \pm 0.07$	$2.02 \pm 0.13$	$1.00 \pm 0.02$	$2 \pm 5$	$1.63 \pm 0.04$	24	$12 \pm 2.6$	$1.16 \pm 0.04$	$709 \pm 29$
QAT 44-2	C-L4477	0.60	100-200	$1.24 \pm 0.06$	$2.02 \pm 0.13$	$0.81 \pm 0.02$	$2 \pm 5$	$1.42 \pm 0.04$	20	$24 \pm 4.3$	$1.68 \pm 0.10$	$1182 \pm 75$

### S3 XRD spectra and sample locations

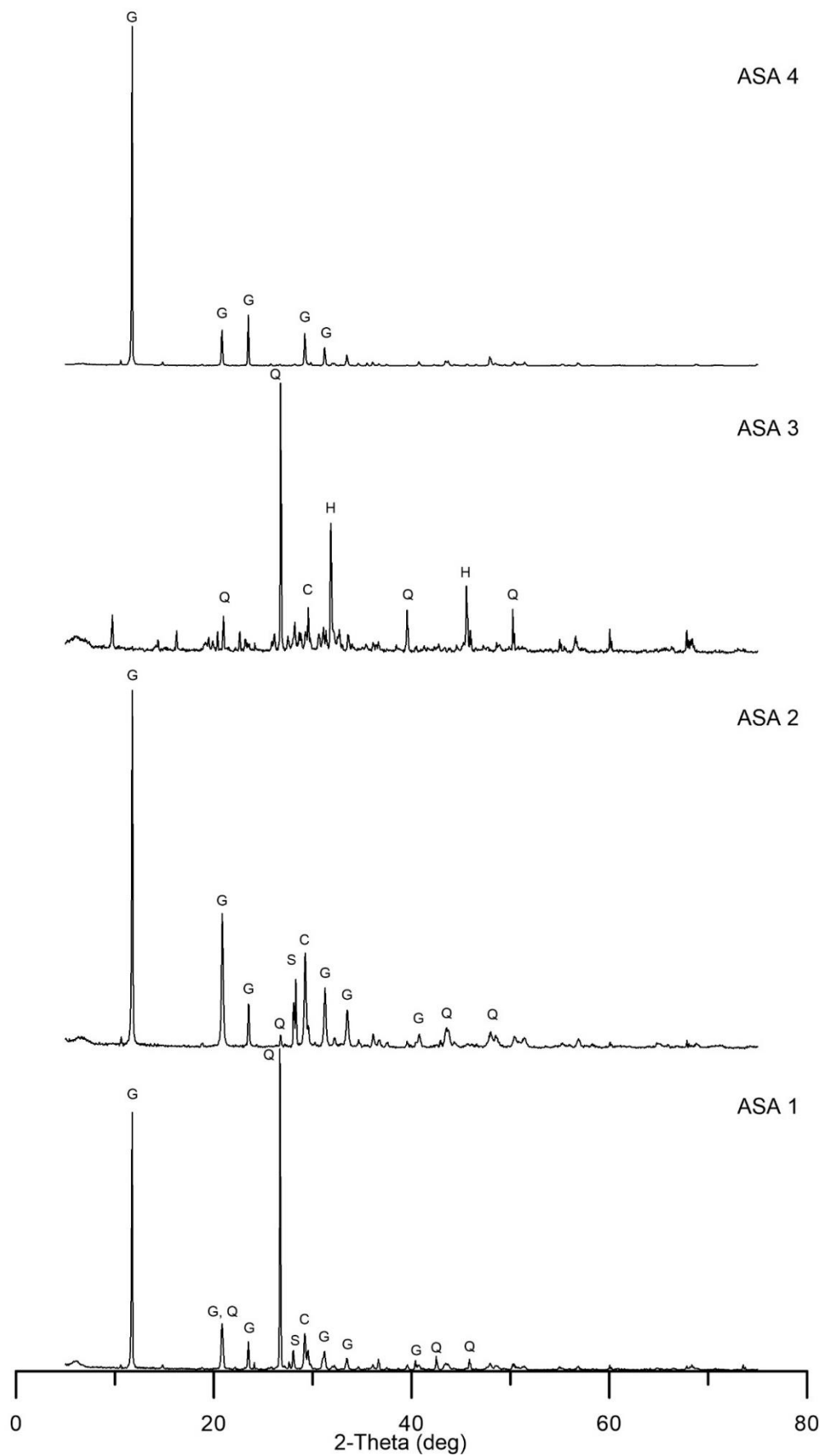


Fig. S5: XRD spectra of surface samples ASA 1–4 (Q=quartz; C=calcite; G=gypsum; H=halite; S=sylvine).

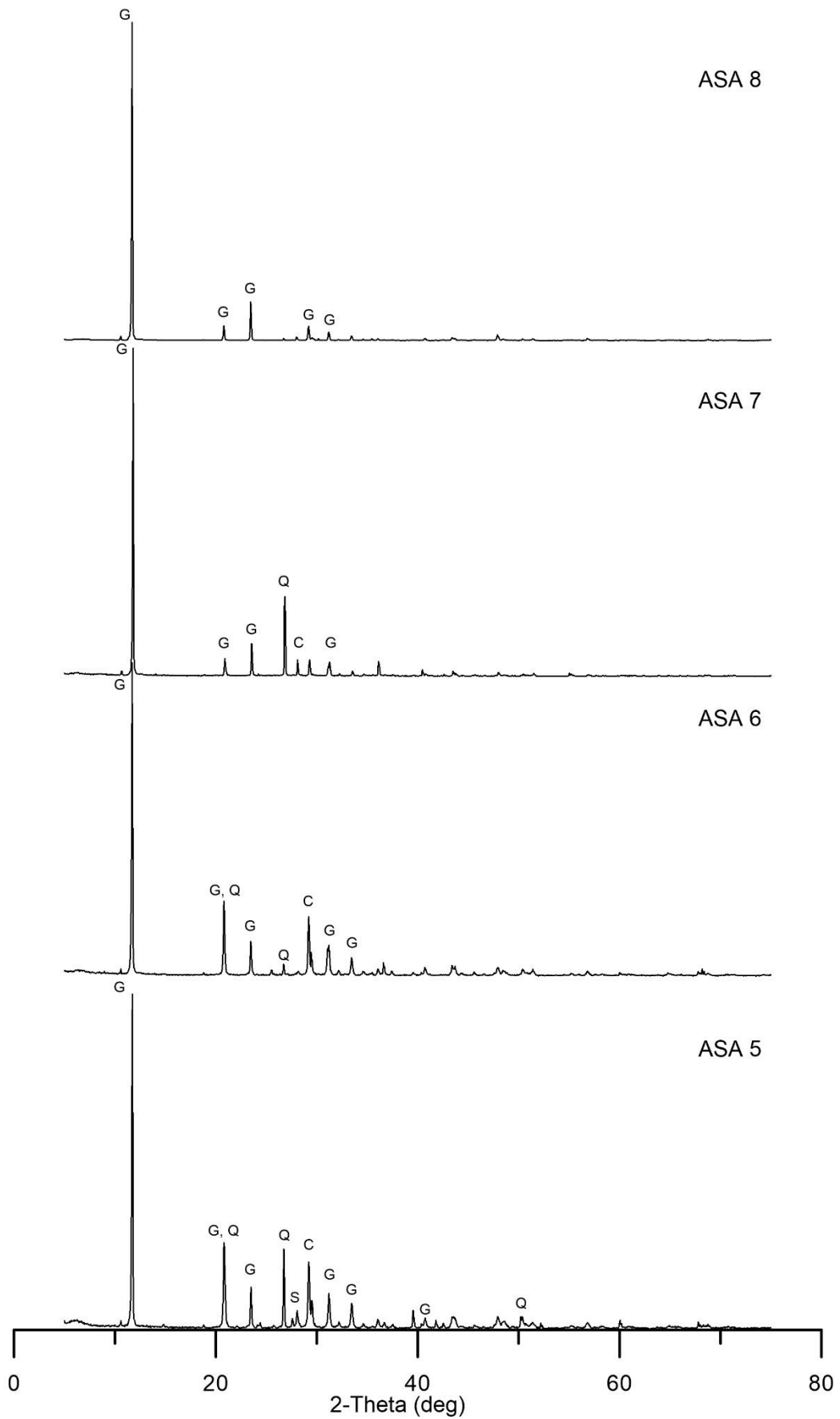


Fig. S6: XRD spectra of surface samples ASA 5–8 (Q=quartz; C=calcite; G=gypsum; S=sylvine).

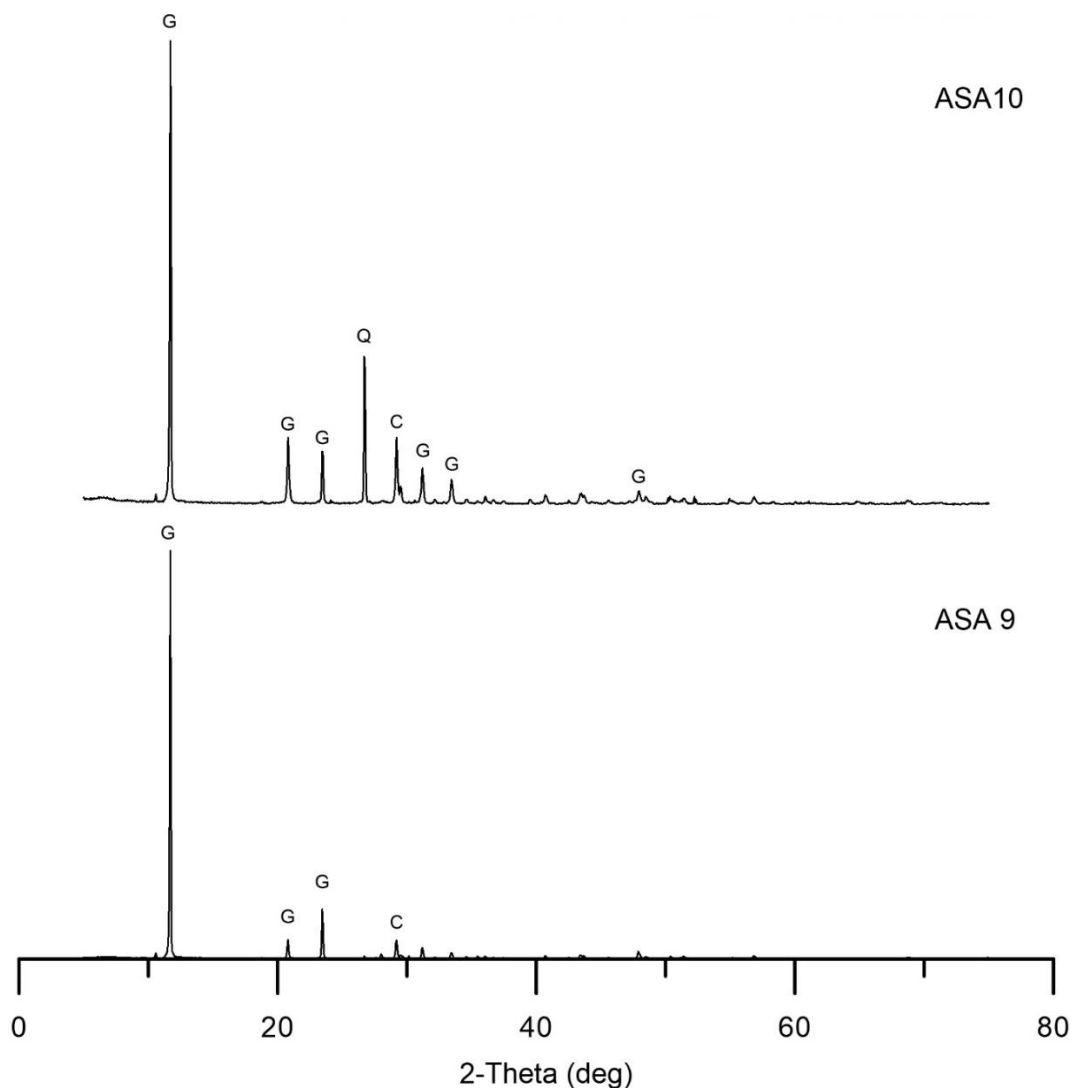


Fig. S7: XRD spectra of surface samples ASA 9 and 10 (Q=quartz; C=calcite; G=gypsum).

Table S2: Location and remarks for surface XRD samples (see Figs. 1, S5–S7).

Site	E	N	Geomorphic unit	Comp	
ASA 1	50.917740	25.2945961	Hummocky sand flats	G,Q,C,S	Relic evaporite crust of a low mound
ASA 2	50.921448	25.2966901	Hummocky sand flats	G,Q,C,S	Thick relic evaporite crust of a low mound
ASA 3	50.918090	25.2942141	Hummocky sand flats	G,Q,C,H	Active gypsum horizon; platy desert roses
ASA 4	50.917730	25.2940301	Hummocky sand flats	G	Pure gypsum crystals from root pseudo-morphs (gypsum precipitated around former rootlets) found at the surface.
ASA 5	50.915290	25.3000181	Round to elongated mounds (northern occurrence)	G,Q,C,S	White, porous, calcite-bearing gypsum from a rather low mound
ASA 6	50.915290	25.3000181	Round to elongated mounds (northern occurrence)	G,Q,C	Similar to ASA 5
ASA 7	50.916878	25.2969381	Wadi channel	G,Q,C	Reddish brown crust, 1-2 cm thick, few larger clasts at the surface
ASA 8	50.911465	25.2816721	Round to elongated mounds (southern occurrence)	G	Thick, relic crust, surface part
ASA 9	50.911465	25.2816721	Round to elongated mounds (southern occurrence)	G,C	Thick, relic crust, bottom part
ASA 10	50.912037	25.2851561	Linear mounds	G,Q	Relic, gypsum crust protecting linear features

## **S4 Geomorphic mapping of the Asaila basin: Systematic description of the landform units (Fig. 2)**

### *S4.1. Higher limestone plateau (c. 13–18 m QVD<sup>1</sup>)*

The Asaila basin is surrounded by the flint-bearing limestone plateaus of the Dammam Formation. These plateaus are covered by a dense hamada surface comprising eroded remnants of *in-situ* limestone and flint (Figs. 3a, S8). The highest flint concentration can be found on the southern plateau, where numerous flint knolls outcrop at the surface, while it is lowest on the eastern plateau, where also the amount of finer material at the surface is higher and, thus, vegetation denser. *Stipa capensis* grass dominates the higher plateaus, while towards the slopes *Zygophyllum qatarense* and *Lycium shawii* occur. The slopes are mostly steep (>35°) to moderately steep (15–35°).

### *S4.2. Rugged higher limestone plateaus, ridges and buttes (c. 8–15 m QVD)*

Towards the basin, the higher limestone plateaus merge into the more dissected, rugged higher limestone plateaus, ridges and buttes. This unit is present all along the basin margin and comprises iconic outliers protruding into the middle limestone plateaus and the basin itself (Figs. 3a, S9). The slopes are mostly moderately steep (15–35°) and covered by slope debris and aeolian sand. Besides the hamada, evaporitic crusts may appear at the surface, in particular in the north. Vegetation density is higher compared to the higher plateau and is dominated by the shrubs *L. shawii* and *Z. qatarense*, *Sclerocephalus arabicus*, as well as grasses *S. capensis* and *Panicum turgidum*.

### *S4.3. Lower limestone plateau (c. 2–8 m QVD)*

Between the higher plateau and the bottom of the depression, there is a distinct plateau level formed by Dammam limestone (Figs. S10–S13), which only in the northeast gives way to a gentle slope (Fig. S10a). In the east, southeast, south and west, the lower limestone plateau is separated from the slopes leading towards the bottom of the depression by a clear topographical step of 1–2 m. It is mostly covered by hamada (Fig. S8), in some parts consolidated by an evaporitic crust. Vegetation is relatively dense and dominated by grasses, while occasional *Acacia tortilis* trees can be found.

### *S4.4. Terraced slope debris*

The slopes of the middle limestone plateaus towards the depression are covered by multimodal slope debris that mainly result from a combination of aeolian sand sedimentation and the gravitational deposition of larger clasts (Fig. 3a). Large limestone clasts characterize the low-inclination surface (2–7°). Vegetation is very sparse.

### *S4.5. Sand ramps*

Along the northeastern margin, short ramps of unimodal sand are being accumulated basinward on top of the slope debris, extending from the edge of the higher and lower limestone plateaus where they may also cover the southern to southeastern slopes of the outliers (Figs. S9, S12). Sand is supplied from locations in the north and delivered by the Shamal wind system. Sand grains saltating over the plateaus and passing their edges feed the ramps as the abrupt topographical change reduces aeolian

---

<sup>1</sup> QVD = Qatar Vertical Datum, defined as the mean sea level 1970–1972; reference mark located at the old airport of Doha

transport competency. Narrowly spaced wind ripples indicate that the sand ramps are actively forming, which prevents the establishment of vegetation. In some places, the sand ramps are covered by collapsing caprock (Fig. S10b).

#### *S4.6. Gravel sheets*

The transition area between the terraced slope debris and the bottom of the depression is occupied by a sand and fine gravel cover with a low concentration of larger clasts (coarse cobbles to fine boulders) (Figs. 3a, S11, S13). It differs from the hamada on the higher limestone plateau in terms of their high percentage of sand. The gravel sheets gently incline towards the center of the depression. Where evaporitic crusts occur at the surface, the gravel sheet forms a terrace with a clear basinward step. Vegetation is very sparse, similar to the terraced slope debris units.

#### *S4.7. Hummocky sand flats*

The gravel sheets often merge into a sand flat with active aeolian dynamics (Fig. S13), indicated by *Z. qatarense* shrubs forming a wide range of sand accumulations from small, narrow and crested leeward dunes up to substantial nebkhas (Figs. S14, S15). These hummocky sand flats cover the major part of the depression. In some cases, the sandy mounds are consolidated by evaporitic crusts, have grown beyond single-shrub-centred nebkha size, and their morphodynamic activity is reduced. Surface samples ASA 1 and 2 show that the crust is made up of gypsum, quartz sand, calcite and minor occurrences of sylvine, an easily soluble salt (Fig. S5, Table S2). In some places, gypsum-based root pseudomorphs (surface sample ASA 4; Fig. S5, Table S2) were found at the surface (Fig. S16), indicating predominant deflation, and in some areas desert roses (platy, circular crystal clusters of gypsum and quartz sand, with minor incorporation of calcite and halite as indicated by surface sample ASA 3; Fig. S5, Table S2) grow actively (Figs. S17, S18). Besides the dense cover of *Z. qatarense*, the hummocky sand flats, comprise grasses such as *P. turgidum* and *Cistanche tubulosa*.

#### *S4.8. Sabkha-type sand flats*

The northwestern and southwestern parts of the depression, characterized by the lowest elevations, comprise sandy, vegetation-free areas with flat, salt- and gypsum-encrusted, sabkha-type surfaces, some even with halite-containing polygonal patterns at the surface (Figs. 3a,b, S19, S20). These are the areas of highest moisture and appear darker in the satellite images (e.g., Fig. S9d).

#### *S4.9. Round to elongated mounds*

In particular in the central southern areas of the Asaila basin, mounds of varying shape and density occur. Their uppermost part is consolidated by evaporitic crusts. The mounds vary from perfectly round, up to 1 m high, to narrow ridges, several tens of metres long (Fig. 3b, S21). Vegetation is generally less dense compared to the hummocky sand flats and mainly comprises *Z. qatarense* and *Aizoon canariense*. The unit has three different subtypes:

- (a) Linear ridges in the southwestern basin, partly cross-cutting, with seemingly random orientation (Fig. S21). In between the ridges, active aeolian deposition occurs. Here, the crust is rather porous, white to light grey and mostly several centimetres thick; surface sample ASA 10 contains gypsum and quartz (Fig. S7, Table S2).

- (b) Round to more elongated, often yardang-type mounds with a long axis aligned to the Shamal corridor (Fig. S22, S23). Active aeolian deposition occurs in between the mounds. The evaporitic crust protecting the mounds is relatively thick (up to 30–40 cm). Its texture ranges from massive (Figs. S25, S26) to porous (Figs. S27, S28) gypsum (surface samples ASA 5, 6, 8, 9), with contributions of quartz sand and calcite (ASA 5, 6, 9), and, only very occasionally, sylvine (ASA 6 [Figs. S6, S7, Table S2]). Boundaries between (a) and (b) may appear gradual.
- (c) Lower density of mounds and only thin, sometimes even absent evaporitic crusts and reduced vegetation cover; the area shares some similarities with and also merges into the sabkha-type sand flats. Some active aeolian deposition occurs in between the mounds (Fig. S24).

#### *S4.10. Wadi and channel*

Two areas inside the basin exhibit unequivocal signs of surface water flows. Extending from the central northern margin and bifurcating towards the centre of the basin is a vegetation-free, linear depression of 10–20 cm (Fig. 5) with a weak, reddish-brown surface crust of gypsum, quartz sand and calcite (Fig. S6, Table S2) with high amounts of clay and silt (Fig. S31).

The eastern end of the Asaila basin is characterized by retrogressive erosion associated with a wadi channel (Figs. S29, S30). The wadi is filled with slope debris and experiences aeolian overprinting in the form of sand ramps (Figs. S12, S29a). However, horizontally bedded platy clasts in a poorly sorted, consolidated sandy matrix and an outwashed channel exposing barren bedrock point to at least episodic surface water flows (Figs. S29a, S30a). Vegetation is dense comprising *A. tortilis* and *L. shawii*.

#### *S4.11. Areas of modern land use*

Besides dirt roads and single tracks crossing the depression, temporary camel and sheep farms are set up in the Asaila basin. At the entrance of the southeastern wadi, a permanent date farm was installed in the 1970s, fed by artificial wells, which is today abandoned (Gerber et al., 2014). North of the date farm, the remains of the Islamic Asaila Fort (Hardy-Guilbert, 1980) are located on an outlier of the higher limestone plateau.

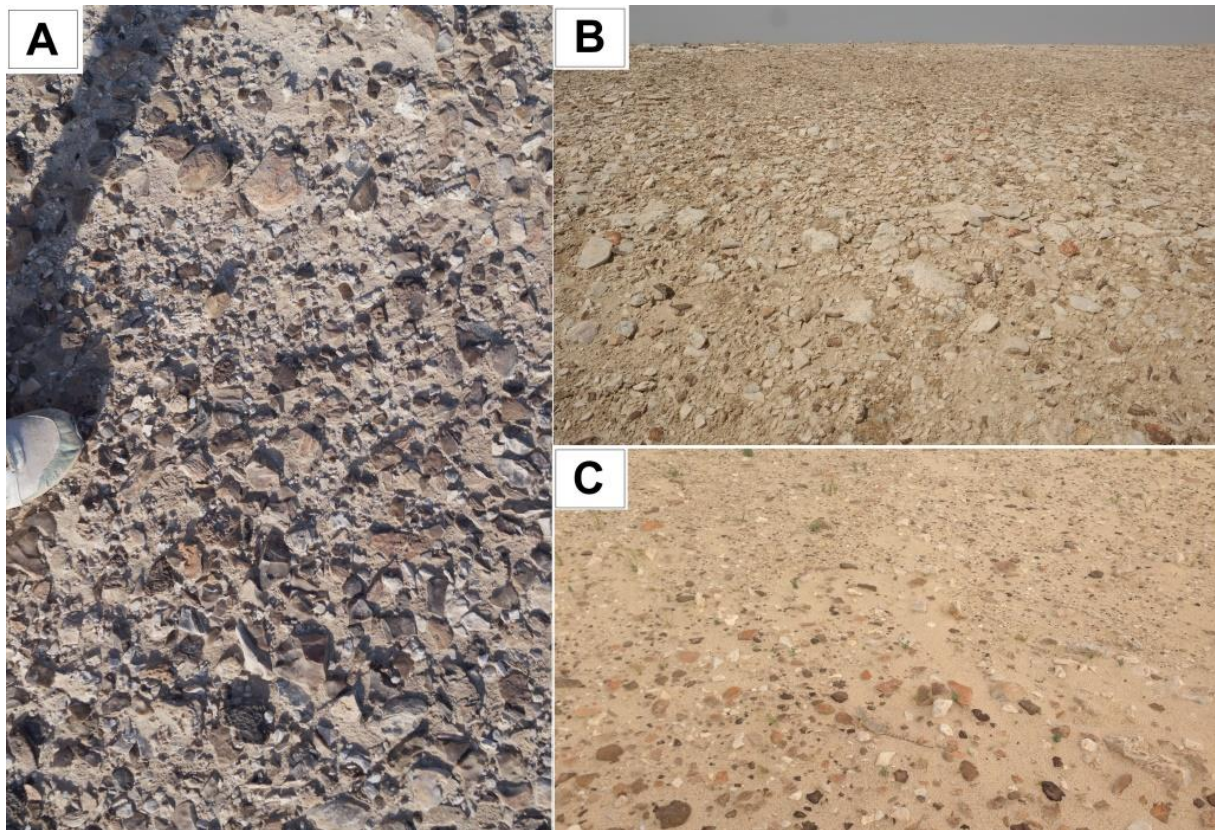


Fig. S8: Typical hamada surfaces of the higher and lower limestone plateaus north (A) and east (B,C) of the Asaila basin.

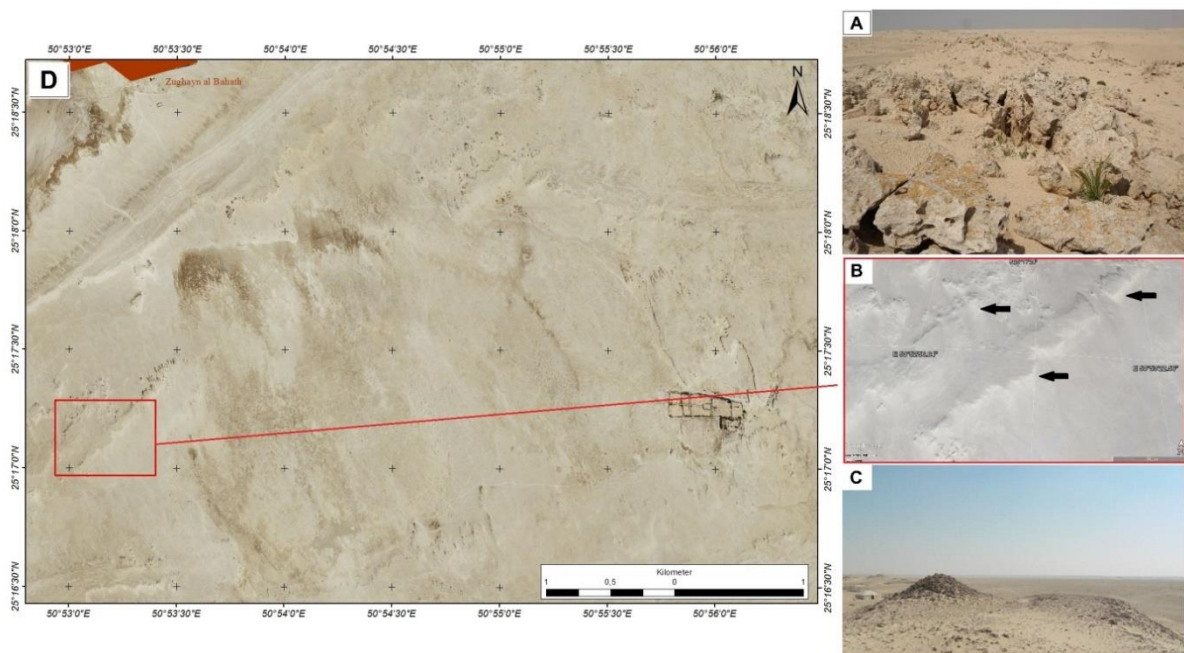


Fig. S9: Rugged higher limestone ridge as part of the plateau unit at the western margin of the Asaila basin (A,D [IKONOS imagery 2004]), with sand ramps along the southeastern edge (light areas in B; Google Earth), where sands driven by the Shamal winds and saltating over the plateau lose support by the wind. (C) Outliers of the higher plateau with evaporitic cementation.



Fig. S10: Different aspects of the lower limestone plateau. (A) View over the area of the magnetic prospection (Figs. 2,4) with the smoothly inclined surface towards the basin created by multimodal, sand-dominated deposition covering the limestone plateau (very similar to the adjacent gravel sheets). (B) Lower Dammam limestone forming the lower limestone plateau in the west of the Asaila basin; the cliff framing the basin is typically masked by a sand ramp.



Fig. S11: Magnetometer prospection (Figs. 2,4) in the environs of the old Acila 36 excavation of Inizan (1988) and Pelegrin and Inizan (2013), at the transition of the incised and sediment-filled lower limestone plateau (densely covered by grasses) and the gravel sheet.



Fig. S12: Sand ramps accumulated against the cliff of the lower limestone plateau in the wadi area of the western Asaila basin.

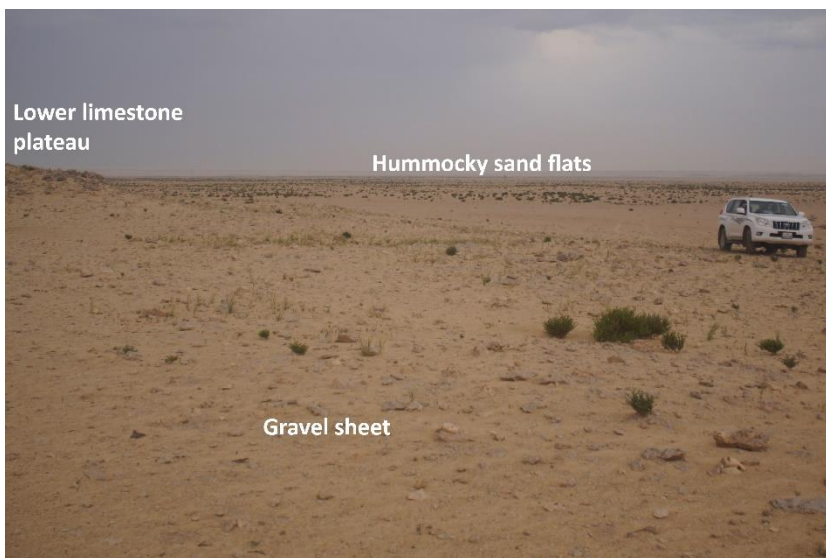


Fig. S13: Transition between the gravel-dominated sheets and hummocky sand flats of the inner basin at the north-western margin of the Asaila basin, downslope of the magnetometer prospecting area (Fig. 2).



Fig. S14: Nebkha field as part of the hummocky sand flat in the centre of the Asaila basin.



Fig. S15: Sand tail (or proto-nebkha) downwind of a *Zygophyllum qatarense* shrub inside the hummocky sand flats.



Fig. S16: Root pseudo-morphs: pure gypsum precipitated around former rootlets (cf. sample ASA 4 in Fig. S5 and Table S2). The fact that they are now exposed and distributed over the surface indicates a predominant deflation regime.



Fig. S17: Desert roses actively growing 20 cm below the surface of the hummocky sand flats.



Fig. S18: Zoom into the horizon of desert roses (up to c. 7–8 cm large plates).



Fig. S19: Sabkha-type sand flats, in some areas showing polygonal surface patterns induced by active halite, carbonate and gypsum precipitation.



Fig. S20: Coring site QAT 63 on the sabkha-type sand flats.



Fig. S21: Linear, crosscutting mounds in the central southern Asaila basin (subtype a in Fig. 2).



Fig. S22: Small field of rounded mounds (subtype b in Fig. 2) in the central northern Asaila basin, merging into the hummocky sand flats, rich in *Z. qatarense*.



Fig. S23: Elongated to rounded mounds in the central southern Asaila basin (subtype b in Fig. 2).



Fig. S24: Lower-density mound field (subtype c in Fig. 2) with very sparse vegetation cover and active aeolian deposition.



Fig. S25: Elongated to rounded mounds in the central southern Asaila basin with moderate vegetation (subtype b in Fig. 2).



Fig. S26: Zoom into the profile in Fig. S25 showing the typical white, relict gypsum crust of c. 15 cm thickness preserving the mounds.



Fig. S27: Profile in rounded mound field of the central northern Asaila basin with thinner, more porous gypsum crust (subtype b in Fig. 2).



Fig. S28: Zoom into the profile of Fig. S27 showing a thinner, more porous and calcite-bearing version of the white gypsum crust preserving the mounds.

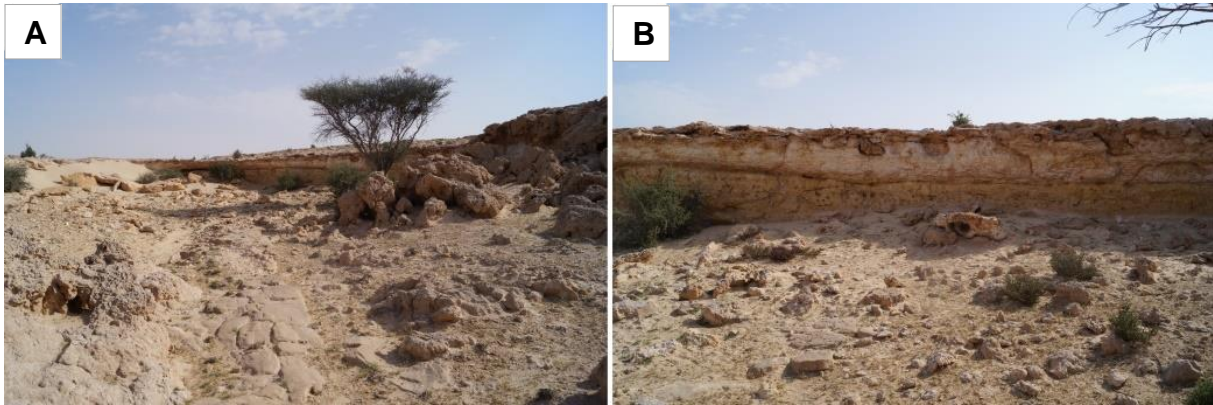


Fig. S29: Wadi of the eastern Asaila basin with traces of recent surface runoff exposing the bedrock in the central part of the picture (A). While downwind of the Shamal, relatively pure sand ramps develop (left background of A), most steep flanks are covered by gravitational talus slopes (B).

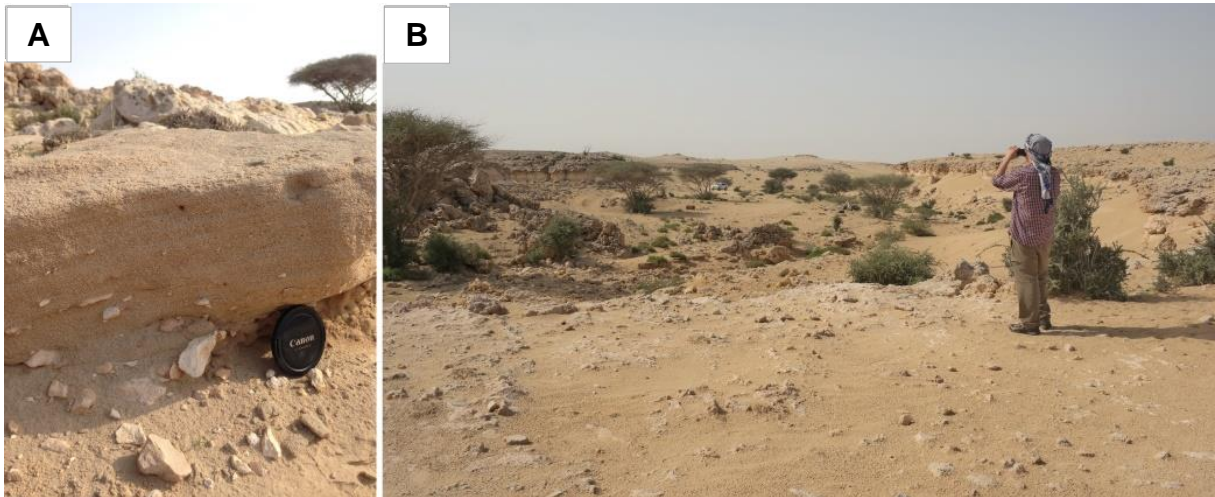


Fig. S30: Laminated bedding of poorly sorted facies with parallel aligned limestone clasts resulting from episodic fluvial activity inside the wadi. The deposit is modern, but weakly cemented by carbonate (A). (B) Overview from the wadi head.

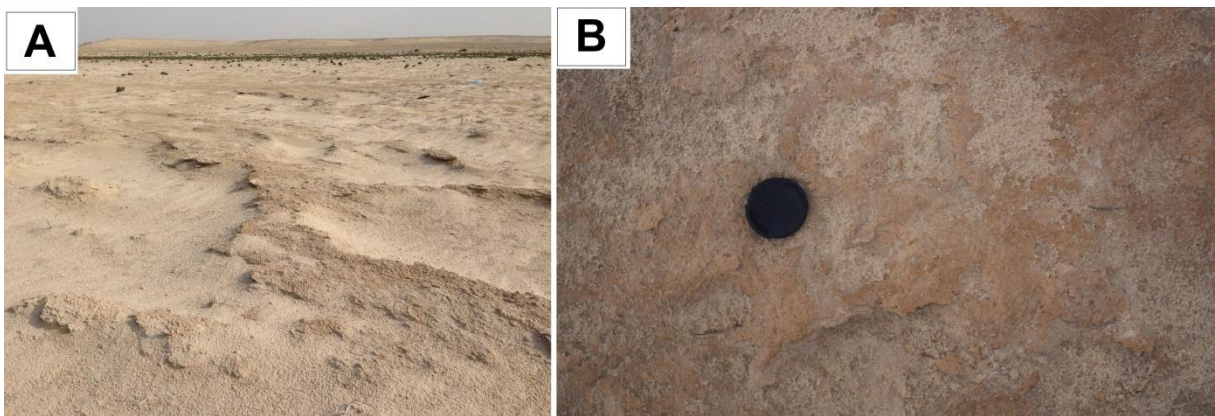


Fig. S31: Shallow, vegetation-free wadi channel (A) with thin, fragmented, reddish brown surface crust (B) entering the Asaila basin in the north (Fig. 5).



Fig. S32: View towards the basin of Jaow Aqeeq from the eastern edge, with temporary standing water (upper left) and the sabkha area (dark brown, framing the water) in the background. The red arrow indicates coring site ASA-C1 (Fig. 7) in the sabkha area.



Fig. S33: Linear corrosion features on a rawdha surface of southern Qatar. The arrow indicates the main Shamal direction (Engel et al., 2018).



Fig. S34: Micro-yardang (long axis <50 cm) inside a rawdha of southern Qatar indicating active deflation mainly induced by the Shamal (white arrow shows the yardang's long axis and the dominant wind direction). Its formation is supported by protection of a small boulder, while the surrounding surface has been lowered by deflation (Engel et al., 2018).

## References

- Durcan, J. A., King, G. E., and Duller, G. A. T.: DRAC: Dose rate and age calculator for trapped charge dating, *Quat. Geochronol.*, 28, 54–61, doi:10.1016/j.quageo.2015.03.012, 2015.
- Engel, M., Boesl, F., and Brückner, H.: Migration of barchan dunes in Qatar—controls of the Shamal, teleconnections, sea-level changes and human impact, *Geosciences*, 8, 240, doi:10.3390/geosciences8070240, 2018.
- Fassbinder, J. W. E.: Seeing beneath the farmland, steppe and desert soil: Magnetic prospecting and soil magnetism, *J. Archaeol. Sci.*, 56, 85–95, doi:10.1016/j.jas.2015.02.023, 2015.
- Fassbinder, J. W. E.: Magnetometry for Archaeology, in: *Encyclopedia of Geoarchaeology*, edited by: Gilbert, A. S., Springer, Dordrecht, 499–514, doi:10.1007/978-1-4020-4409-0\_169, 2017.
- Galbraith, R. F., Roberts, R. G., Laslett, G. M., Yoshida, H., and Olley, J. M.: Optical dating of single grains of quartz from Jinmium rock shelter, northern Australia, Part I: experimental design and statistical models, *Archaeometry*, 41, 339–364, doi:10.1111/j.1475-4754.1999.tb00987.x, 1999.
- Gerber, C., Drechsler, P., Yasin-Meier, D., Brückner, H., Engel, M., Meier, D.M.P., Götzelt, T., Daitche, J., Hörwarthner, D., Lienig, A., Reising, R., and Tiltmann, S.: The German-Qatari South Qatar Survey Project: The 2012–2013 Season, *Z. Orient Archäol.*, 7, 248–275, 2014.
- Guérin, G., Mercier, N., and Adamiec, G.: Dose-rate conversion factors: update, *Ancient TL*, 29, 5–8, 2011.
- Hardy-Guilbert, C.: Recherches sur la période islamique au Qatar, in: *Mission archéologique à Qatar, tome 1*, edited by Tixier, J., Doha, 111–128, 1980.

Inizan, M.-L. (Ed.): *Préhistoire à Qatar. Mission archéologique française à Qatar (2)*, Éditions Recherche sur les Civilisations, Paris, France, 1988.

Murray, A. S., and Wintle, A. G.: The single aliquot regenerative dose protocol: potential for improvements in reliability, *Radiat. Meas.*, 37, 377–381, doi:10.1016/S1350-4487(03)00053-2, 2003.

Pelegrin, J., and Inizan, M.-L.: Soft hammerstone percussion use in bidirectional blade-tool production at Acila 36 and in bifacial knapping at Shagra (Qatar), *Arab. Archaeol. Epigr.*, 24, 79–86, doi:10.1111/aae.12016, 2013.

Prescott, J. R., and Hutton J. T.: Cosmic ray contributions to dose rates for luminescence and ESR dating: Large depths and long-term time variations, *Radiat. Meas.*, 23, 497–500, doi:10.1016/1350-4487(94)90086-8, 1994.